

# PoP-Net: Pose over Parts Network for Multi-Person 3D Pose Estimation from a Depth Image

Yuliang Guo\*

Zhong Li†

Zekun Li‡

Xiangyu Du

Shuxue Quan

Yi Xu

{yuliang.guo, zhong.li, zekun.li, xiangyu.du, shuxue.quan, yi.xu}@oppo.com  
OPPO US Research Center

## ABSTRACT

In this paper, a real-time method called PoP-Net is proposed to predict multi-person 3D poses from a depth image. PoP-Net learns to predict bottom-up part representations and top-down global poses in a single shot. Specifically, a new part-level representation, called Truncated Part Displacement Field (TPDF), is introduced which enables an explicit fusion process to unify the advantages of bottom-up part detection and global pose detection. Meanwhile, an effective mode selection scheme is introduced to automatically resolve the conflicting cases between global pose and part detections. Finally, due to the lack of high-quality depth datasets for developing multi-person 3D pose estimation, we introduce Multi-Person 3D Human Pose Dataset (MP-3DHP) as a new benchmark. MP-3DHP is designed to enable effective multi-person and background data augmentation in model training, and to evaluate 3D human pose estimators under uncontrolled multi-person scenarios. We show that PoP-Net achieves the state-of-the-art results both on MP-3DHP and on the widely used ITOP dataset, and has significant advantages in efficiency for multi-person processing. To demonstrate one of the applications of our algorithm pipeline, we also show results of virtual avatars driven by our calculated 3D joint positions. MP-3DHP Dataset and the evaluation code have been made available at: <https://github.com/oppo-us-research/PoP-Net>.

## 1 INTRODUCTION

Human pose estimation plays an important role in a wide variety of applications, and there is a rich pool of literature for human pose estimation methods. Categorizations of existing methods can be made from different dimensions. There are methods mostly relying on a single image to predict human poses [15, 20, 27] and others based on multiple cameras [4, 24]. Some methods are capable of predicting multiple poses [3, 14] while others are focusing on single person [17, 20, 27]. Some methods estimate 3D poses [12, 19, 25, 28] while others only predict 2D poses [17, 18, 27]. Methods can also be differentiated by the input, while most methods use RGB images [2, 3, 15, 18], some use depth maps [13, 26, 28]. Specifically, this paper focuses on multi-person 3D pose estimation from a depth image.

In the era of deep learning, a large pool of Deep Neural Networks (DNN)-based methods have been developed for multi-person pose estimation. Ideas from existing literature can be generally categorized into three prototypical trends. The simplest idea is to directly extend a single-shot object detector [11, 21, 22] with additional pose attributes, so that the network can output human poses. Such single-shot regression can be very efficient, but has low part accuracy, as shown in Figure 2 (Yolo-Pose+), because a long-range inference for

\*Contact Author, the work was done when Guo was with OPPO.

†Contact Author.

‡The work was done when Li was an intern with OPPO.

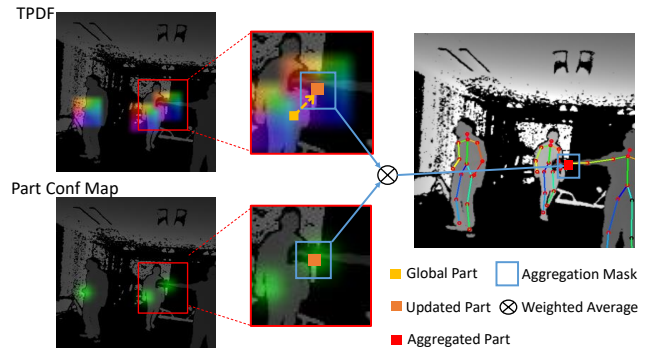


Figure 1: **Our paradigm.** Part representations and global poses predicted from PoP-Net are explicitly fused via utilizing Truncated-Part-Displacement-Field (TPDF). A part predicted from the global pose is dragged towards a more precise bottom-up part position following a displacement vector. More reliable part position is further estimated via a part-confidence-weighted average of TPDF within the aggregation mask.

part locations is involved in a center-relative pose representation. The second type builds on a two-stage pipeline where the first stage detects object bounding boxes, and the second stage estimates the pose within each [6, 18, 28]. Two-stage methods can be very accurate, as shown in Figure 2 (Yolo-A2J), but not as efficient when more human beings appear in an image. In addition, more sophisticated design is required to solve the compatibility issue between pose estimation and bounding box detection [6, 21]. The third idea is to detect human poses from part<sup>1</sup> detection and association [3, 9, 13, 14, 16]. Although part detection can be rather efficient, solving the part association problem is usually time consuming. OpenPose [3] gained its popularity for introducing an efficient solution to solve the association, resulting in a network benefiting from both the single-shot pipeline with high efficiency and the part-based dense representation with high positional precision. However, a pure bottom-up method does not have a global sense, so that it is rather sensitive to occlusion, truncation, and ambiguities in symmetric limbs (Figure 2 OpenPose+). Moreover, dependency on the bipartite matching in assembling parts presents the part predictions from differentiable integration with global context reasoning, which may systematically block a solution from end-to-end training [14].

Developing a depth image-based multi-person 3D pose estimation from a well-established RGB image-based 2D method [3, 18, 23] is conceptually simple for two reasons: some schemes to handle multi-person detection can be shared; 3D information is partially available from the input [5, 28]. As a result, a depth image-based approach may not necessarily require as many sophisticated designs as methods aiming to estimate 3D poses from a single RGB image [14, 15].

<sup>1</sup>The definitions of 'part' and 'joint' are interchangeable in this paper.

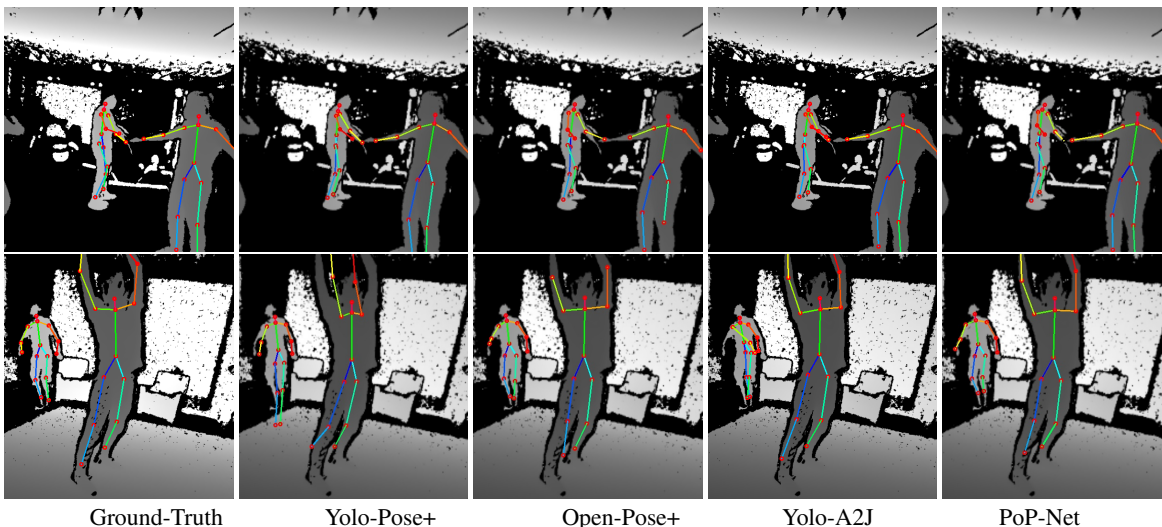


Figure 2: **Visual comparison of prototypical methods:** methods are compared on two examples from MP-3DHP testing set.

However, RGB-based methods and depth-based methods usually focus on different challenges. While some RGB-based methods spend more effort in differentiating people cluttered in a large scene [2, 3], depth-based methods [13, 28] focus more on recovering highly accurate 3D poses of fewer people presented in a closer range. In practice, to develop a depth-based method that robustly predicts 3D poses in a multi-person scenario is very challenging due to noisy depth inputs and heavy occlusions.

In this paper, we present a method called Pose-over-Parts Network (**PoP-Net**) to estimate multiple 3D poses from a depth image. As illustrated in Figure 1, the main idea of PoP-Net is to explicitly fuse the predicted bottom-up parts and top-down global poses<sup>2</sup>. This fusion process is enabled by a new intermediate representation, called Truncated-Part-Displacement-Field (TPDF), which is a vector field that records the vector pointing to the closest part location at every 2D position. TPDF is utilized to guide a structural valid global pose towards more positionally precise part location so that the advantages of global pose and local part detection can be naturally unified.

At the same time, we release a comprehensive depth dataset, named Multi-Person 3D Human Pose Dataset (MP-3DHP), to facilitate the development of 3D pose estimation methods generalizable to novel background and unobserved multi-person configurations in real-world applications. Although there are a decent amount of RGB datasets [1, 8, 10] in prior art, there are limited high-quality depth datasets. The released dataset is constructed to cover most of the essential aspects of visual variance related to 3D human pose estimation, and particularly to promote the development of multi-person methods.

The contribution of this paper is four fold. First, we introduce an efficient framework that predicts multiple 3D poses in a single shot. Second, we propose a new part-level representation called TPDF, which enables an explicit fusion of global poses and part-level representations. Third, we introduce a mode selection scheme that automatically resolves the conflicting cases between local and global predictions. Finally, we release a comprehensive depth image-based dataset to facilitate the development of multi-person 3D pose estimation methods applicable to real-world challenges.

<sup>2</sup>Poses predicted from a single-shot network where each pose contains a full set of body parts

## 2 POSE-OVER-PARTS NETWORK

In this paper, we present a new method, called Pose-over-Parts Network (PoP-Net), for multi-person 3D pose estimation from a depth image. Our method first uses an efficient single-shot network to predict part-level representations and global poses, and then fuses the positionally precise part detection and structurally valid global poses in an explicit way.

The pipeline of PoP-Net is composed of a backbone network, a global pose network, and three functional branches: heatmap branch, depth branch, and TPDF branch, as illustrated in Figure 3. The two-stage split-and-merge design is inspired by OpenPose [3] and mostly follows the simplified version applied to depth input [13]. PoP-Net outputs three sets of part maps from the second stage of functional branches and an anchor-based global pose map from the global pose network.

Supposing a human body includes  $K$  body parts, the heatmap branch outputs a set of part confidence maps  $\{H_j\}_{j=1}^{K+1}$ , where each  $H_j$  from the first  $K$  maps indicates the confidence of a body part occurring at each discrete location, and the last indicates background confidence. The depth branch outputs a set of maps  $\{D_j\}_{j=1}^K$ , where each  $D_j$  encodes the depth values associated with part  $j$ .

The core of our method is a new part-level representation called Truncated Part Displacement Field (TPDF). For each part type  $j$ , TPDF records a displacement vector pointing to the *closest* part instance at every 2D position. The TPDF branch outputs TPDFs represented in a set of  $x$ -axis displacement maps  $\{X_j\}_{j=1}^K$  and a set of  $y$ -axis displacement maps  $\{Y_j\}_{j=1}^K$ . The novelty of the proposed TPDF is two fold: (1) it encodes the displacement field involving multiple parts of the same type in a single map, and (2) a *truncated* effective range is adopted, which is critical for training CNN models that are able to handle multi-body scenarios. If truncated range is not applied to the part displacement field involving part instances from multiple bodies, the training of convolutional kernels will be confused by image patches similar in appearance but associated with highly different vectors, because a pair of displacement vectors whose origins are close to each other but pointing to different part instances may have large difference in  $X, Y$  values. The effectiveness of applying the truncated range is analyzed in detail in Section 4.3.

Compared with previous methods which predict person-wise part displacements [18, 28], TPDF operates at image level. In consequence, PoP-Net not only handles multiple bodies in one pass but also happens to be less sensitive to proposal error. While compared

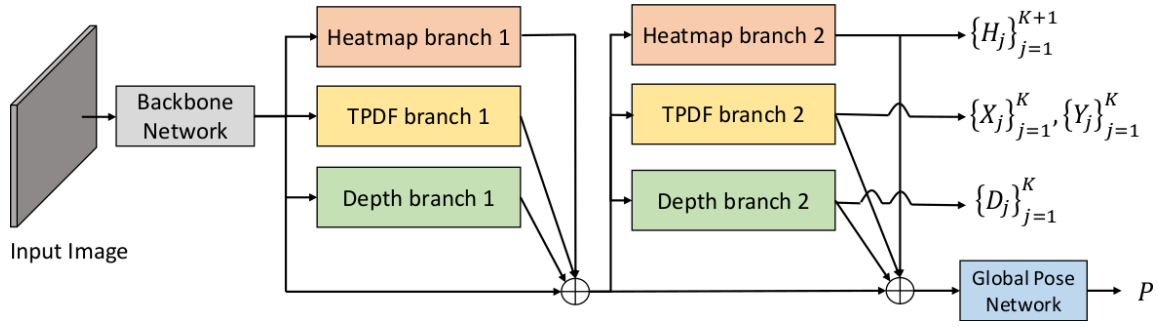


Figure 3: **PoP-Net** is composed of a backbone network, three functional branches, and a global pose network. The functional branches are organized in two stages with split and merge. PoP-Net outputs three part-level maps and a global pose map.

with the Part Affinity Field introduced in OpenPose [3], TPDF is free from the heavy bipartite matching process, and uses a simple fusion process to take advantage of both global poses and bottom-up part detections. As a result, PoP-Net shows increased robustness to handling truncation, occlusion and multi-person conflict compared with OpenPose.

Finally, a global pose map  $P$  is regressed from the global pose network. The global pose network is a direct extension from Yolo2 [22], where both bounding box attributes and additional 3D pose attributes are regressed with respect to the anchors associated with each grid. A set of predicted global poses are then extracted via conducting NMS on the global pose map  $P$ .

## 2.1 Training

PoP-Net is trained end-to-end via minimizing the total loss  $\mathcal{L}$  which is the sum of heatmap loss  $\mathcal{L}_h$ , depth loss  $\mathcal{L}_d$ , TPDF loss  $\mathcal{L}_t$ , and global pose loss  $\mathcal{L}_p$ . As shown in Figure 3, losses corresponding to the functional branches are contributed from multiple stages of the network. Specifically, the loss function can be written as:

$$\begin{aligned} \mathcal{L} &= \mathcal{L}_h + \mathcal{L}_d + \mathcal{L}_t + \mathcal{L}_p \\ \mathcal{L}_h &= \sum_{s=1}^S \sum_{j=1}^{K+1} \|H_j^s - H_j^*\|_2^2 \\ \mathcal{L}_d &= \sum_{s=1}^S \sum_{j=1}^K W_j^d \cdot \|D_j^s - D_j^*\|_2^2 \\ \mathcal{L}_t &= \sum_{s=1}^S \sum_{j=1}^K W_j^t \cdot (\|X_j^s - X_j^*\|_2^2 + \|Y_j^s - Y_j^*\|_2^2) \\ \mathcal{L}_p &= W^P \cdot \|P - P^*\|_2^2 \end{aligned}$$

where  $s$  is the stage index, and  $S$  indicates the total number of stages.  $H_j^*$ ,  $D_j^*$ ,  $X_j^*$ ,  $Y_j^*$ , and  $P^*$  indicate the ground-truth maps while  $W_j^d$ ,  $W_j^t$ , and  $W^P$  indicate the point-wise weight maps in the same dimension as the corresponding ground-truth maps. Specifically, no weight maps are applied to heatmap loss so that the foreground and background samples are treated with equal importance.

The architecture of each network component and the preparation process of ground-truth maps and weight maps are illustrated in detail in Appendix A. In summary, the backbone and the heatmap branch follow the structure proposed in the simplified OpenPose for depth data [13]. The depth and TPDF branches adopt the same number of layers as the heatmap branch but with customized feature dimensions to balance the efficiency and robustness. The global pose network follows a similar architecture as the layers after the backbone in Yolo2 [22], and uses a similar anchor-based representation.

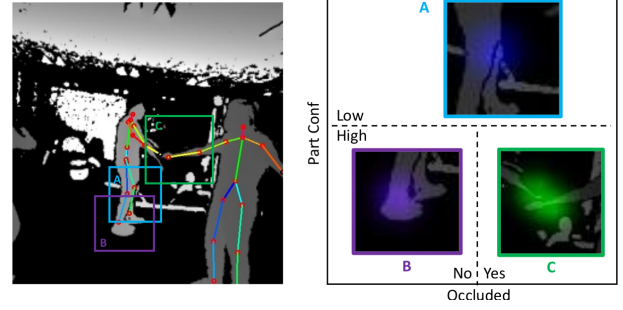


Figure 4: **Conflicting cases to resolve in fusion.** Part confidence maps for the marked regions are visualized to illustrate three conflicting cases to resolve. A: The confidence of left knee is low. B: The confidence of right foot is high without ambiguity. C: The confidence of occluded right hand is high but hallucinated by the same part from another person.

## 2.2 Fusion process

TPDF enables an explicit fusion of part representations and global poses. As illustrated in Figure 1, a 2D part predicted from a global pose located at  $(x_j, y_j)$  is updated to a new position  $(\hat{x}_j, \hat{y}_j)$  following the displacement vector in the predicted TPDF of part  $j$ , such that  $\hat{x}_j = x_j + X_j(x_j, y_j)$ ,  $\hat{y}_j = y_j + Y_j(x_j, y_j)$ . To improve accuracy, weighted aggregation is later applied to estimate the final 2D position  $\{(\hat{x}_j, \hat{y}_j)\}_{j=1}^K$  and depth  $\{\hat{Z}_j\}_{j=1}^K$ , as illustrated in Figure 1. Specifically,  $X_j$ ,  $Y_j$ , and  $D_j$  within a mask  $M$  centered at the updated integer position  $(\lfloor \hat{x}_j \rfloor, \lfloor \hat{y}_j \rfloor)$  is averaged by using  $H_j$  as aggregation weights, which leads to the following equations:

$$\hat{x}_j = \lfloor \hat{x}_j \rfloor + \frac{\sum_{(u,v) \in M} H_j(u,v) \cdot X_j(u,v)}{\sum_{(u,v) \in M} H_j(u,v)} \quad (1)$$

$$\hat{y}_j = \lfloor \hat{y}_j \rfloor + \frac{\sum_{(u,v) \in M} H_j(u,v) \cdot Y_j(u,v)}{\sum_{(u,v) \in M} H_j(u,v)} \quad (2)$$

$$\hat{Z}_j = \frac{\sum_{(u,v) \in M} H_j(u,v) \cdot D_j(u,v)}{\sum_{(u,v) \in M} H_j(u,v)}. \quad (3)$$

Predicted  $\{(\hat{x}_j, \hat{y}_j)\}_{j=1}^K$  and  $\{\hat{Z}_j\}_{j=1}^K$  are transformed to 3D positions given known camera intrinsic parameters.

## 2.3 Resolving conflicting cases

There are conflicting cases when multiple human bodies occlude each other or a global pose falls out of the effective range of a TPDF. To resolve them, a mode selection scheme is carefully designed. The scheme utilizes the part confidence maps  $\{H_j\}_{j=1}^{K+1}$  from the

heatmap branch and the part visibility attributes from the global pose network.

As illustrated in Figure 4, there are in total three cases to consider respectively: (A) when the part confidence  $H_j$  is low at a global part position, the global detection is used directly, which is usually observed when the position of a part is not accessible due to truncation or occlusion; (B) when the part confidence is high and no occlusion from another instance of the same part is involved, the presented fusion process is applied; and (C) a challenging case may occur when the part confidence is high but is impacted by occlusion from another instance of the same part type. Fortunately, since the part depth map is prepared following a  $z$ -buffer rule, a significant difference between the global part depth and the part depth map will be observed in this case. Therefore, part visibility attributes  $\{v_j\}_{j=1}^K$  can be used as indicators of case (C), which can be integrated into the global pose representation. At last, the visual results of PoP-Net are shown in Figure 5 on a set of multi-person testing samples.

### 3 MP-3DHP: MULTI-PERSON 3D HUMAN POSE DATASET

Due to the lack of high-quality depth datasets for 3D pose estimation, we constructed Multi-Person 3D Human Pose Dataset (MP-3DHP) to facilitate the development of 3D pose estimation targeting real-world multi-person challenges. There are a few existing depth datasets for human pose estimation, but the data quality and diversity is rather limited. DIH [13] and K2HPD [26] include a decent amount of data but are limited to 2D poses. ITOP [5] is a widely tested depth dataset for 3D pose estimation. However, data from ITOP is strictly limited to single person, clean background, and low diversity in object scales, camera angles, and pose types.

MP-3DHP is designed to effectively cover the essential variations in human poses, object scales, camera angles, truncation scenarios, background scenes, and dynamic occlusion. Because collecting sufficient data to fully represent multi-person configurations combined with different background scenes is intractable due to combinatorial explosion, real data is only collected to cover the variations not achievable from data composition or data augmentation. Specifically, our training data collection focuses on single-person data involving varying poses, different object scales, varying camera ray angles, and additional background-only data covering different types of scenes. The remaining types of data variation are covered via data composition and data augmentation utilizing collected human segments. The testing set focuses on multi-person data under uncontrolled real-world scenarios. Figure 6 shows examples from the training set, the background scenes and the multi-person testing set respectively.

Set	Img	Sbj	Loc	Ori	Act	Sn	L+
train	176828	13	4+	4	10+	1	seg
val	32719	2	4+	4	10+	1	seg
bg	8680	0	0	0	0	8	no
test	4484	5	0	0	free	4	mp

Table 1: **MP-3DHP summary.** The total number of images (Img), human subjects (Sbj), recording locations (Loc), self-orientations (Ori), action types (Act), scenes (Sn) are summarized. Additional label type (L+) indicates whether a set has segmentation (seg) or multi-person (mp) labels.

#### 3.1 Construction procedure

We utilized Azure Kinect to record human depth videos and automatically extracted 3D human poses associated with each depth image. Overall, 20 human candidates were involved in the recording procedure; 15 of them were recorded individually to construct the training set, while the remaining five were recorded in multi-person sessions to produce the multi-person testing set. For the training set,

each candidate was recorded with a clean background in four trials at four different locations within the camera frustum. In each trial, a candidate was asked to perform 10 predetermined actions while facing four different orientations spanning  $360^\circ$  and an additional short sequence of free-style movements towards the end. A classic graph-cut based method was applied to produce human segments for the training set. In addition, background images were recorded separately with moderate camera movements from eight different scenes. For the testing set, the remaining five people were recorded while performing random actions with different combinations in four different scenes. Table 1 shows the statistics of our MP-3DHP dataset.

To collect reliable 3D pose ground-truth, human annotations are integrated into our pseudo-automatic data collecting system to sift out those unqualified samples. Specifically, we used two calibrated and synchronized cameras mounted on a solid bar in data capture, one is from Azure Kinect and the other is from a commercial cellphone. A 3D pose output from Azure Kinect is only selected as ground-truth when its projections to both views are visually correct.

## 4 EXPERIMENTS

We experimentally substantiate the superiority of PoP-Net in depth image-based multi-person 3D pose estimation on two datasets, under two evaluation metrics, compared to prior state-of-the-art methods.

### 4.1 Experimental setup

#### 4.1.1 Datasets

A depth-based 3D pose estimation method is evaluated on two benchmarks: the MP-3DHP and ITOP [5] datasets. MP-3DHP includes highly diverse 3D human data and provides reliable human segments to enable background augmentation and multi-person augmentation. The evaluation on MP-3DHP aims to determine a method’s capability in handling real-world challenges in multi-person 3D pose estimation. Meanwhile, ITOP is a widely tested dataset for single-person 3D pose under highly controlled environment. We report results on ITOP to compare with prior state-of-the-arts on a simplified task.

#### 4.1.2 Evaluation metric

A method is evaluated in PCK and mAP with different focuses. First, PCK is a measurement that focuses on pose estimation without considering redundant detections. In our experiments, PCK is calculated as the average percentage of accurate key points on the best-matched predictions to the ground-truth poses, where the best match is based on the IOU between 2D bounding boxes. Second, the mAP metric introduced in MPII [1] dataset is applied, which integrates both the object detection and pose estimation accuracy in an overall score. For both PCK and mAP, 0.5-head size rule is applied for 2D while 10-cm rule is applied for 3D.

#### 4.1.3 Competing methods

A few prototypical methods have been compared with our method: (a) Yolo-Pose+ represents a typical top-down method, which is a pose estimation network extended from yolo-v2 [22] and implemented by us; (b) Open-Pose+ is a pure bottom-up method that is an extension from RPM [13], a simplified version of OpenPose [3]) that we extended with a depth branch to predict 3D poses; (c) A2J [28] represents the state-of-the-art two-stage pose estimation from a depth image.

To conduct a fair comparison, Yolo-Pose+, Open-Pose+, and PoP-Net are implemented using as many identical modules as possible. Specifically, Yolo-Pose+ is composed of the backbone network, the global pose network used for PoP-Net, and five additional intermediate  $3 \times 3$  convolutional layers with  $256d$  features in between. Open-Pose+ integrates the same backbone network, heatmap branch, depth branch as PoP-Net, and an additional Part Affinity Field (PAF)

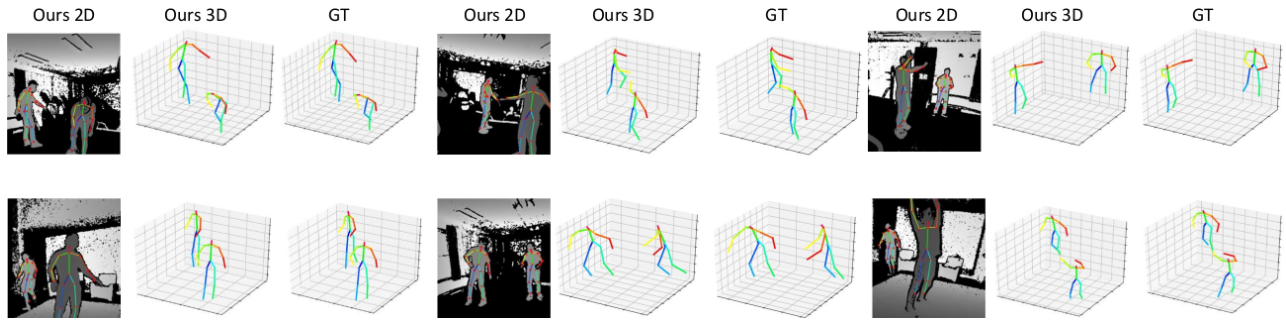


Figure 5: **PoP-Net visual results.** Predictions in 2D, 3D, and the ground-truth are visualized on six examples from MP-3DHP.

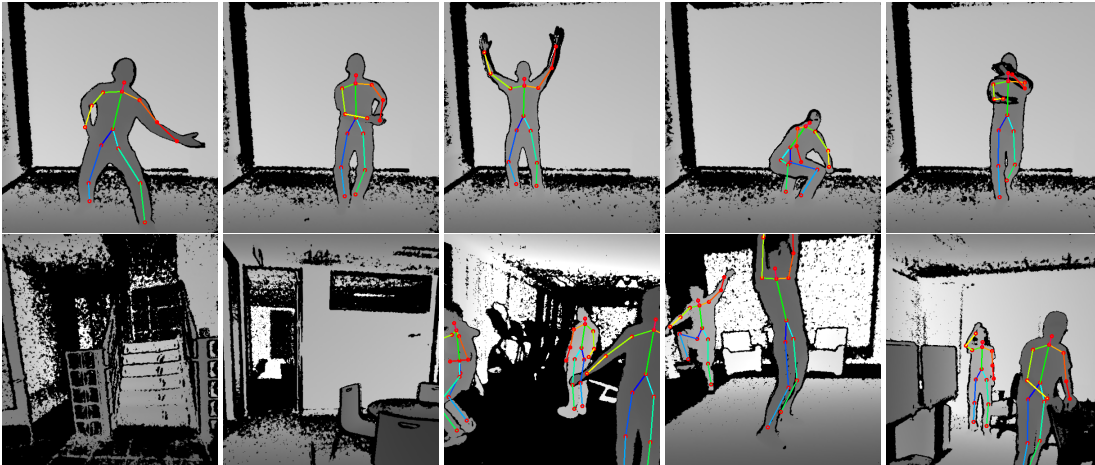


Figure 6: **MP-3DHP examples.** (Top) Five single-person examples recorded from different locations from the training set. (Bottom) Two examples of background scenes, and three examples from multi-person testing set.

branch proposed in [3]. The post process of Open-Pose+ follows the original work to use bipartite matching upon PAF to assemble detected parts into human bodies, and in addition reads the depth branch output to produce 3D poses. For A2J [28], we use the identical network presented in the original paper to reproduce the results. Because A2J needs to work with given bounding-boxes for the multi-person case, we provide the predicted bounding boxes from Yolo-Pose+ to A2J so that the bounding-box quality is comparable to the other methods.

#### 4.1.4 Implementation details

The input depth images are resized to  $224 \times 224$  for Yolo-Pose+, Open-Pose+, and PoP-Net. The images are cropped and resized to  $288 \times 288$  for A2J. Yolo-Pose+, Open-Pose+, PoP-Net are trained via standard SGD optimizer for 100 epochs, while A2J is trained via Adam optimizer following the original paper. Yolo-Pose+, Open-Pose+, and PoP-Net use two anchors with size  $6 \times 12$  and  $3 \times 6$ , respectively. Following the study provided in [3], all the functional branches both in PoP-Net and Open-Pose+ use  $S = 2$  stages for an optimal balance in efficiency and accuracy. PoP-Net uses the TPDF truncated range  $r = 2$  in training, an optimal setting found in ablation study. At inference, the aggregation mask  $M$  used in fusion is practically defined as a  $5 \times 5$  square. An identical data augmentation process is applied to the training of each method. The basic data augmentation process is applied to both MP-3DHP and ITOP, which includes random rotation, flipping, cropping, and a specific depth augmentation described in Appendix B. While the multi-person augmentation is only applied on MP-3DHP.

## 4.2 MP-3DHP dataset

On MP-3DHP dataset, each method is trained on the training set with multi-person augmentation on top of basic data augmentation. Given the provided human segments, background augmentation can be applied by superimposing the human mask region from a training image onto a randomly selected background image. Meanwhile, multi-person augmentation can also be applied by superimposing multiple human segments onto a random background scene following  $z$ -buffer rule, which is described in more detail in Appendix C. In testing, a method is evaluated on four different datasets representing different levels of challenges: (1) the validation set (**Simple**), (2) the background augmented (**BG Aug**) set constructed from validation set, (3) the multi-person augmented (**MP Aug**) set constructed from validation set, and (4) the real multi-person (**MP Real**) testing set including challenging real-world recordings.

### 4.2.1 Quantitative comparison

PoP-Net is compared with the other methods on MP-3DHP. As observed in Table 2, PoP-Net achieves the state-of-the-art almost on every testing set, and significantly surpasses other methods under the most challenging metric: 3D mAP on the MP Real test. Open-Pose+ shows marginal advantages in 2D mAP in certain cases because it could benefit from higher recall by recovering isolated parts without seeing a whole body. However Open-Pose+ is more erroneous in depth prediction under occlusion due to its pure bottom-up pipeline, hence its 3D mAP drops significantly. A2J, on the other hand, shows marginal advantage in 3D PCK in certain tests, which can be interpreted as that the global weighted aggregation could leverage the full context within ROI to infer the depth of an occluded part. However,

A2J appears to be rather sensitive to the quality of predicted ROIs; therefore its mAP performance is not optimal.

Test	Method	2D PCK	3D PCK	2D mAP	3D mAP
Simple	Yolo-Pose+	0.957	0.910	0.926	0.847
	Open-Pose+	<b>0.967</b>	0.915	<b>0.967</b>	<b>0.893</b>
	Yolo-A2J	0.959	<b>0.924</b>	0.936	0.868
	PoP-Net	<b>0.978</b>	<b>0.947</b>	<b>0.974</b>	<b>0.926</b>
BG Aug	Yolo-Pose+	0.956	0.904	0.923	0.834
	Open-Pose+	0.911	0.916	<b>0.969</b>	<b>0.885</b>
	Yolo-A2J	<b>0.964</b>	<b>0.927</b>	0.941	0.871
	PoP-Net	<b>0.982</b>	<b>0.947</b>	<b>0.977</b>	<b>0.924</b>
MP Aug	Yolo-Pose+	0.872	0.777	0.799	0.651
	Open-Pose+	<b>0.887</b>	0.765	<b>0.870</b>	0.667
	Yolo-A2J	0.876	<b>0.819</b>	0.803	<b>0.707</b>
	PoP-Net	<b>0.906</b>	<b>0.808</b>	<b>0.863</b>	<b>0.708</b>
MP Real	Yolo-Pose+	0.734	0.607	0.616	0.449
	Open-Pose+	0.805	0.641	<b>0.802</b>	0.558
	Yolo-A2J	<b>0.837</b>	<b>0.724</b>	0.744	<b>0.574</b>
	PoP-Net	<b>0.839</b>	<b>0.708</b>	<b>0.799</b>	<b>0.606</b>

Table 2: **Evaluation on MP-3DHP.** Competing methods are evaluated on four testing sets. The best method is marked in bold black while the second best is marked in blue.

#### 4.2.2 Qualitative comparison

In order to demonstrate that PoP-Net achieves the state-of-the-art and the proposed MP-3DHP represents real-world challenges, we compare the predicted poses from competing methods on a set of challenging cases. As shown in Figure 8, we demonstrate visual comparison on: (1) an example including a target human captured far beyond the observation range in the training; (2-3) examples having severe background occlusion; (4-5) examples including multi-person occlusion and considerable truncation; and (6) an example with unobserved poses from training. As observed, PoP-Net in general is more reliable across all these cases. However, all methods failed on some most challenging cases. Such observation indicates that there is still huge room for improvement towards a robust approach in real-world challenges.

### 4.3 Ablation study

An ablation study has been conducted on MP-3DHP to analyze the effectiveness of PoP-Net components and the specific data augmentation methods. Because our motivation is to solve multi-person 3D pose estimation, we only conduct the ablation study on MP-3DHP, which to our knowledge is the only dataset providing multi-person 3D pose labels.

#### 4.3.1 Effectiveness of fusing pose and parts

The effectiveness of fusing part representations and global poses has been studied. As shown in Table 3, evaluation has been done on four different testing sets from MP-3DHP, and separately on: (1) the 2D global poses predicted from the global pose network (**2D Glb**), (2) the final 2D poses after fusion (**2D Fuse**), (3) the 3D global poses predicted from the global pose network (**3D Glb**), and (4) the 3D poses computed from 2D fused poses and predicted depth of parts (**3D Fuse**). In addition, the upper bound of 3D poses computed from ground-truth 2D poses and predicted depth (**3D UB**) has been reported to illustrate the importance of depth prediction.

As observed, 2D and 3D poses after fusion constantly improve upon the direct predictions from the global pose network, and the margin increases on more challenging testing sets. Meanwhile, the accuracy of 3D pose prediction drops more significantly compared with 2D pose prediction on more challenging sets, where the upper bound is still far from ideal. Improving depth prediction under multi-person occlusion should be a main focus in a future work.

Metric	Test	2D Glb	2D Fuse	3D Glb	3D Fuse	3D UB
PCK	Simple	0.968	0.978	0.939	0.947	0.956
	BG Aug	0.970	0.982	0.938	0.947	0.953
	MP Aug	0.898	0.906	0.794	0.808	0.846
	MP Real	0.798	0.839	0.681	0.708	0.756
mAP	Simple	0.963	0.974	0.917	0.926	0.931
	BG Aug	0.965	0.977	0.915	0.924	0.927
	MP Aug	0.849	0.863	0.701	0.708	0.735
	MP Real	0.755	0.799	0.582	0.606	0.622

Table 3: **Ablation study on fusing pose and parts.**

#### 4.3.2 Effectiveness of data augmentation

The effectiveness of the depth augmentation (**D Aug**) method and the composition augmentation (**C Aug**) are analyzed. The depth augmentation considers different ranges of  $a$ . The composition augmentation includes background augmentation (**BG Aug**) and multi-person augmentation (**MP Aug**). Experiments have been conducted with a focus on the multi-person real testing set as these augmentation methods were motivated towards this ultimate task. However, the data augmentation methods are not limited to PoP-Net, but applicable to any method trained on MP-3DHP.

D Aug	C Aug	2D PCK	3D PCK	2D mAP	3D mAP
0.7-1.7	w\o	0.411	0.246	0.374	0.158
0.7-1.7	BG Aug	0.769	0.634	0.748	0.550
<b>0.7-1.7</b>	<b>MP Aug</b>	<b>0.839</b>	<b>0.708</b>	<b>0.799</b>	<b>0.606</b>
w\o	MP Aug	0.610	0.481	0.617	0.427
0.5-2.5	MP Aug	0.835	0.648	0.785	0.508

Table 4: **Ablation study on data augmentation.**

As observed from Table 4, background augmentation leads to a significant improvement (over 30%) compared to the baseline without any composition augmentation (2nd row vs. 1st row). Multi-person augmentation (3rd row) leads to another leap (about 5%). On the other hand, the specific depth augmentation also plays a critical role in improving the robustness (about 18% increase in 3D mAP, 3rd row vs. 4th row), especially for objects from unobserved scales. However, further extension of the depth augmentation range leads to a drawback in 3D mAP (10%, 5th row vs. 3rd row), which is reasonable because the depth augmentation method can not fully simulate the data far beyond the original captured distance.

#### 4.3.3 Effectiveness of PoP-Net components

To find an optimal configuration of the pipeline, we analyzed the effects of the truncated range  $r$  on TPDF, the effectiveness of depth prediction (**D Pred**) and the conflict resolving scheme (**Sol C**), as reported in Table 5.

A few important conclusions can be drawn from the results. First, depth prediction plays an important role in recovering reliable 3D poses, which leads to about 30% improvements in 3D metrics compared with using the raw depth directly. Second, the introduced

Sol C	D Pred	TPDF	2D PCK	3D PCK	2D mAP	3D mAP
w	w\o	$r = 2$	0.839	0.418	0.799	0.293
w\o	w	$r = 2$	0.833	0.696	0.797	0.598
w	w	$r = 1$	0.827	0.678	0.782	0.560
<b>w</b>	<b>w</b>	<b><math>r = 2</math></b>	<b>0.839</b>	<b>0.708</b>	<b>0.799</b>	<b>0.606</b>
w	w	$r = 3$	0.825	0.681	0.777	0.567
w	w	$r = 5$	0.821	0.670	0.780	0.557
w	w	$r = 10$	0.797	0.654	0.755	0.543
w	w	$r = \text{inf}$	0.647	0.549	0.581	0.443

Table 5: **Ablation study on PoP-Net components.**

conflict resolving scheme leads to about 1% improvement in 3D metrics. Third, applying an appropriate truncated range is critical in learning reliable models to predict part displacement vectors in multi-person scenarios. On the one hand, if the range is too limited, a global pose may not fall in the effective range of TPDF so that the positional accuracy can not be improved. On the other hand, a displacement field without truncation ( $r=\text{inf}$ ) or with large truncated range would confuse the learning. As illustrated in Figure 7, near those sharp boundaries, similar image patches could be associated with drastically different flow vectors. This leads to a degenerate regression problem.

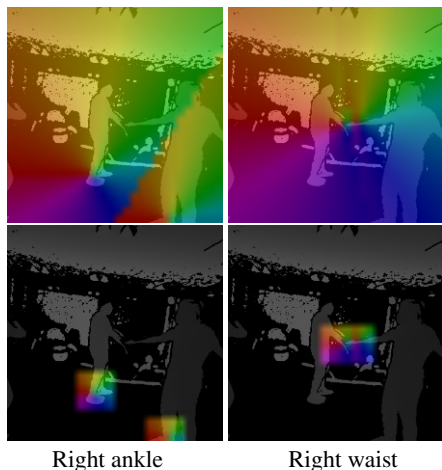


Figure 7: **PDF vs. TPDF.** Full-range PDF examples (top) are compared with the TPDF (bottom) with truncated range  $r = 2$  at  $\frac{h}{8} \times \frac{w}{8}$  feature resolution. Fields associated with the right ankle and right waist channels are visualized on the same depth image.

#### 4.4 ITOP dataset

PoP-Net is compared with competing methods on ITOP dataset. Because ITOP dataset is limited to single-person and clean background, PCK and mAP measurements are mostly identical. Therefore, we only report PCK metrics on ITOP dataset. To conduct a fair comparison, a method is trained and tested under two setups separately. One is based on provided ground-truth bounding boxes and the other directly uses the full image, as shown in Table 6. It can be observed that PoP-Net consistently outperforms Open-Pose+ and Yolo-Pose+ by a significant margin. Compared with A2J, PoP-Net is slightly worse in 3D and better in 2D, which is consistent with the PCK results reported on MP-3DHP.

Exp Setup	Method	2D PCK	3D PCK
GT Bbox	A2J	0.905	<b>0.891</b>
	PoP-Net	<b>0.914</b>	0.882
Full Image	Yolo-Pose+	0.833	0.787
	Open-Pose+	<b>0.876</b>	0.778
	Yolo-A2J	0.873	<b>0.854</b>
	PoP-Net	<b>0.890</b>	<b>0.843</b>

Table 6: **Evaluation on ITOP dataset (front-view).** Methods are evaluated on ITOP dataset with and without GT bounding boxes.

#### 4.5 Running speed analysis

The efficiency of a method is measured in a few different metrics. First, the network complexity is measured in **MACs (G)**, which directly relates to the network inference time. Second, a method’s average running time on an image including a single person (**SP**) is

reported in milliseconds per image (*ms/im*). This metric considers not only network inference time, but also the essential pre-process to provide bounding boxes or the post-process to extract human poses. Third, a method’s average running time on images including multiple people (**MP**) is also reported in milliseconds per image (*ms/im*). Finally, a method’s average running speed on images including multiple people is measured by *fps* which is equivalent to the metric in *ms* per image on MP data. Every method has been tested on a single RTX 2080Ti GPU, and is evaluated in all the metrics as shown in Table 7.

	Yolo-Pose+	Open-Pose+	A2J	PoP-Net
MACs(G)	4.4	6.7	16.6	6.2
SP (ms/im)	4.5	20	14	11
MP (ms/im)	4.5	21	32	11
MP (fps)	223	48	32	91

Table 7: **Running time analysis on multi-person data.**

As observed from MACs (G) scores, Yolo-Pose+ has the lightest network, while A2J has significantly more complex network compared with others. However, consider the pipeline running time, Open-Pose+ is much slower than the others on single-person images. This indicates that the part association post-process involved in Open-Pose+ is a much heavier process compared with the simple post-process used in Pop-Net. On the other hand, although A2J uses a more complex network, it almost has no post-processing cost so that its efficiency on single-person images is even better than Open-Pose+. Finally, as observed from multi-person pipeline running time and speed, the efficiency of A2J drops significantly while the other single-shot methods are not affected. Overall, PoP-Net shows significant advantages in efficiency, which almost triples A2J and doubles Open-Pose+ in multi-person scenarios.

## 5 CONCLUSION

In this paper, we introduce PoP-Net for multi-person 3D pose estimation from a depth image. PoP-Net predicts part maps and global poses in a single pass and explicitly fuses them via utilizing the proposed Truncated Part Displacement Field (TPDF). Conflicting cases are effortlessly resolved in a rule-based process given part visibility and confidence out of the network. Meanwhile, a comprehensive 3D human depth dataset called MP-3DHP is constructed to facilitate the development of models for real-world multi-person challenges. In experiments, PoP-Net achieves state-of-the-art results on MP-3DHP and ITOP datasets with significant advantage in 3D mAP and running speed in processing multi-person data.

### Acknowledgements

This work was supported by OPPO US Research Center.



Figure 8: Visual comparison of competing methods on challenging cases.

## REFERENCES

- [1] M. Andriluka, L. Pishchulin, P. V. Gehler, and B. Schiele. 2d human pose estimation: New benchmark and state of the art analysis. In *IEEE Conference on Computer Vision and Pattern Recognition (CVPR)*, pp. 3686–3693, 2014.
- [2] A. Benzine, F. Chabot, B. Luvison, Q. C. Pham, and C. Achard. Pandanet: Anchor-based single-shot multi-person 3d pose estimation. In *2020 IEEE/CVF Conference on Computer Vision and Pattern Recognition, CVPR 2020, Seattle, WA, USA, June 13-19, 2020*, pp. 6855–6864. IEEE, 2020.
- [3] Z. Cao, T. Simon, S. Wei, and Y. Sheikh. Realtime multi-person 2d pose estimation using part affinity fields. In *IEEE Conference on Computer Vision and Pattern Recognition (CVPR)*, pp. 1302–1310, 2017.
- [4] A. Elhayek, E. de Aguiar, A. Jain, J. Tompson, L. Pishchulin, M. Andriluka, C. Bregler, B. Schiele, and C. Theobalt. Marconi - convnet-based marker-less motion capture in outdoor and indoor scenes. *IEEE Trans. Pattern Anal. Mach. Intell.*, 39(3):501–514, 2017.
- [5] A. Haque, B. Peng, Z. Luo, A. Alahi, S. Yeung, and F. Li. Towards viewpoint invariant 3d human pose estimation. In *14th European Conference Computer Vision (ECCV)*, pp. 160–177, 2016.
- [6] K. He, G. Gkioxari, P. Dollár, and R. B. Girshick. Mask R-CNN. In *IEEE International Conference on Computer Vision (ICCV)*, pp. 2980–2988, 2017.
- [7] K. He, X. Zhang, S. Ren, and J. Sun. Deep residual learning for image recognition. In *IEEE Conference on Computer Vision and Pattern Recognition (CVPR)*, pp. 770–778, 2016.
- [8] C. Ionescu, D. Papava, V. Olaru, and C. Sminchisescu. Human3.6m: Large scale datasets and predictive methods for 3d human sensing in natural environments. *IEEE Trans. Pattern Anal. Mach. Intell.*, 36(7):1325–1339, 2014.
- [9] U. Iqbal and J. Gall. Multi-person pose estimation with local joint-to-person associations. In *European Conference on Computer Vision Workshops*, pp. 627–642, 2016.
- [10] T. Lin, M. Maire, S. J. Belongie, J. Hays, P. Perona, D. Ramanan, P. Dollár, and C. L. Zitnick. Microsoft COCO: common objects in context. In *13th European Conference on Computer Vision (ECCV)*, pp. 740–755, 2014.
- [11] W. Liu, D. Anguelov, D. Erhan, C. Szegedy, S. E. Reed, C. Fu, and A. C. Berg. SSD: single shot multibox detector. In *14th European Conference on Computer Vision (ECCV)*, pp. 21–37, 2016.
- [12] J. Martinez, R. Hossain, J. Romero, and J. J. Little. A simple yet effective baseline for 3d human pose estimation. In *IEEE International Conference on Computer Vision (ICCV)*, pp. 2659–2668, 2017.
- [13] Á. Martínez-González, M. Villamizar, O. Canévet, and J. Odobez. Real-time convolutional networks for depth-based human pose estimation. In *IEEE/RSJ International Conference on Intelligent Robots and Systems (IROS)*, pp. 41–47, 2018.
- [14] D. Mehta, O. Sotnychenko, F. Mueller, W. Xu, M. Elgharib, P. Fua, H. Seidel, H. Rhodin, G. Pons-Moll, and C. Theobalt. Xnect: real-time multi-person 3d motion capture with a single RGB camera. *ACM Trans. Graph.*, 39(4):82, 2020.
- [15] D. Mehta, S. Sridhar, O. Sotnychenko, H. Rhodin, M. Shafiei, H. Seidel, W. Xu, D. Casas, and C. Theobalt. Vnect: real-time 3d human pose estimation with a single RGB camera. *ACM Trans. Graph.*, 36(4):44:1–44:14, 2017.
- [16] A. Newell, Z. Huang, and J. Deng. Associative embedding: End-to-end learning for joint detection and grouping. In I. Guyon, U. von Luxburg, S. Bengio, H. M. Wallach, R. Fergus, S. V. N. Vishwanathan, and R. Garnett, eds., *Annual Conference on Neural Information Processing Systems*, pp. 2277–2287, 2017.
- [17] A. Newell, K. Yang, and J. Deng. Stacked hourglass networks for human pose estimation. In B. Leibe, J. Matas, N. Sebe, and M. Welling, eds., *14th European Conference on Computer Vision (ECCV)*, pp. 483–499, 2016.
- [18] G. Papandreou, T. Zhu, N. Kanazawa, A. Toshev, J. Tompson, C. Bregler, and K. Murphy. Towards accurate multi-person pose estimation in the wild. In *IEEE Conference on Computer Vision and Pattern Recognition (CVPR)*, 2017.
- [19] G. Pavlakos, X. Zhou, and K. Daniilidis. Ordinal depth supervision for 3d human pose estimation. In *IEEE Conference on Computer Vision and Pattern Recognition (CVPR)*, pp. 7307–7316, 2018.
- [20] G. Pavlakos, X. Zhou, K. G. Derpanis, and K. Daniilidis. Coarse-to-fine volumetric prediction for single-image 3d human pose. In *IEEE Conference on Computer Vision and Pattern Recognition (CVPR)*, pp. 1263–1272, 2017.
- [21] J. Redmon, S. K. Divvala, R. B. Girshick, and A. Farhadi. You only look once: Unified, real-time object detection. In *IEEE Conference on Computer Vision and Pattern Recognition (CVPR)*, pp. 779–788, 2016.
- [22] J. Redmon and A. Farhadi. YOLO9000: better, faster, stronger. In *IEEE Conference on Computer Vision and Pattern Recognition (CVPR)*, pp. 6517–6525, 2017.
- [23] S. Ren, K. He, R. B. Girshick, and J. Sun. Faster R-CNN: towards real-time object detection with region proposal networks. *IEEE Trans. Pattern Anal. Mach. Intell.*, 39(6):1137–1149, 2017.
- [24] H. Rhodin, N. Robertini, D. Casas, C. Richardt, H. Seidel, and C. Theobalt. General automatic human shape and motion capture using volumetric contour cues. In *14th European Conference on Computer Vision (ECCV)*, pp. 509–526, 2016.
- [25] B. Tekin, I. Katircioglu, M. Salzmann, V. Lepetit, and P. Fua. Structured prediction of 3d human pose with deep neural networks. In *British Machine Vision Conference (BMVC)*, 2016.
- [26] K. Wang, S. Zhai, H. Cheng, X. Liang, and L. Lin. Human pose estimation from depth images via inference embedded multi-task learning. In *ACM Conference on Multimedia Conference*, pp. 1227–1236, 2016.
- [27] S. Wei, V. Ramakrishna, T. Kanade, and Y. Sheikh. Convolutional pose machines. In *IEEE Conference on Computer Vision and Pattern Recognition (CVPR)*, pp. 4724–4732, 2016.
- [28] F. Xiong, B. Zhang, Y. Xiao, Z. Cao, T. Yu, J. T. Zhou, and J. Yuan. A2J: anchor-to-joint regression network for 3d articulated pose estimation from a single depth image. In *IEEE/CVF International Conference on Computer Vision (ICCV)*, pp. 793–802, 2019.

## A REGRESSION NETWORKS

The network architecture and ground truth preparation for each component are described in detail.

### A.1 Backbone network

The backbone network is implemented to include layers 0-2 from ResNet-34 [7] for general image encoding. It outputs a  $\frac{w}{8} \times \frac{h}{8} \times 128$  feature map, where  $h$  and  $w$  indicate height and width of an input image respectively. We choose to maintain  $8 \times$  downsampling level in the following functional branches to make part-level inference both efficient and capable of handling human parts at a distance.

### A.2 Heatmap branch

The heatmap branch is designed to predict  $K + 1$  confidence maps corresponding to  $K$  body part and the background. The heatmap branch is made of five  $3 \times 3$  convolutional layers as illustrated in Figure 9. It is worth noting that every convolutional layer mentioned in our method is followed by BN and ReLU layers. To prepare ground-truth part confidence maps  $\{H_j^*\}_{j=1}^{K+1}$ , we adopt the same method introduced in OpenPose [3], which applies a Gaussian filter at each part location.

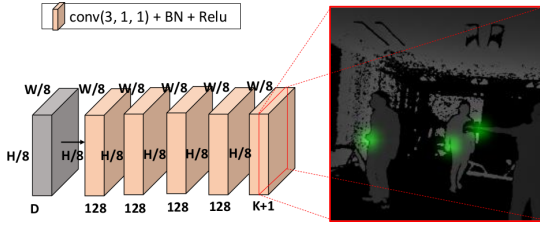


Figure 9: **Heatmap branch.** The heatmap branch predicts  $K$  confidence maps for body parts with an additional map for background.

### A.3 Depth branch

The depth branch predicts part-wise depth maps, which is meaningful in relieving the effect from raw depth artifacts and in recovering the true depth of a part under occlusion. The network is made of five convolutional layers whose specific architecture is shown in Figure 10.

To prepare ground-truth depth maps  $\{D_j^*\}_{j=1}^K$ , each map is initialized with the resized raw depth input. The depth values within a 2-pixel-radius disk centered at each part  $j$  are overridden with the ground-truth depth of part  $j$ , as illustrated in Figure 10. In a multi-person scenario, if a 2D grid position is occupied by masks of more than one part instance, the writing of depth values follows a standard  $z$ -buffer rule where the smallest depth value is recorded. In addition, the weight maps  $\{W_j^d\}_{j=1}^K$  are prepared in the same dimension as the ground-truth depth maps. We use weight 0.9 for a foreground grid while 0.1 for the background.

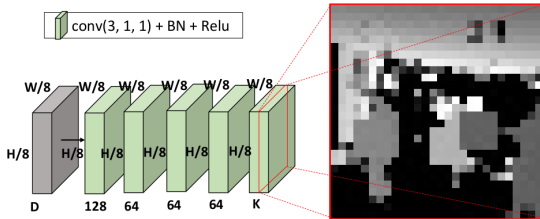


Figure 10: **Depth branch.** The depth branch outputs  $K$  depth maps for  $K$  body parts, respectively.

### A.4 TPDF branch

TPDF maps are predicted from the TPDF branch implemented following the architecture as shown in Figure 11. During ground-truth preparation,  $\{X_j^*\}_{j=1}^K$  and  $\{Y_j^*\}_{j=1}^K$  are prepared so that the displacement vector at a 2D position points to the closest part position. Specifically, the displacement vector is only non-zero within the truncated range ( $r = 2$ ) from each part position, as shown in Figure 11. The preparation of weight maps  $\{W_j^t\}_{j=1}^K$  is similar to the process for the depth branch. However, the weights within the truncated mask is set to 1.0 and the rest is set to strict 0.

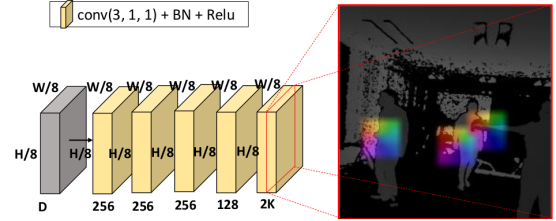


Figure 11: **TPDF branch.** The TPDF branch outputs  $2K$  maps of displacement vectors  $\{X_j^t\}_{j=1}^K$ ,  $\{Y_j^t\}_{j=1}^K$ . The field visualization follows the optical flow standard.

### A.5 Global pose network

The global pose network predicts a global pose map from concatenated features from the backbone and functional branches. The network includes four convolutional layers where the first is followed by a max pooling to cast the feature map to  $16 \times$  downsampling level, as shown in Figure 12.

The ground-truth preparation process is similar to Yolo2 [22]. Specifically, the ground-truth global pose map  $P^*$  is prepared so that each grid records five bounding box attributes and a set of pose attributes  $\{(dx_j^a, dy_j^a, Z_j^a, v_j^a)\}_{j=1}^K$  of the ground-truth pose for each associated anchor  $a$ . Specifically,  $(dx_j^a, dy_j^a)$  indicates the 2D offsets of part  $j$  from the anchor center,  $Z_j^a$  indicates the 3D part depth, and  $v_j^a$  indicates the visibility of part  $j$ . The value of  $v_j^a$  is assigned to 1 when the depth from a global pose part  $Z_j^a$  is different from the corresponding depth branch ground-truth in  $D_j$ , otherwise it is assigned to 0. The weight map  $W^p$  is prepared in the same dimension as  $P^*$ . For the dimensions corresponding to bounding box probabilities, 0.9 is applied to the grids associated with ground truth, while 0.1 is assigned to the rest. For the other dimensions, the weights are strictly assigned to 1 or 0. The weight map is designed in such a way because the detection task related to  $p_b$  considers both foreground and background while the regression task to other attributes focuses only on foreground.

## B DEPTH AUGMENTATION

Given camera intrinsic parameters, the captured depth map, and associated 2D/3D poses, novel depth maps and associated 2D/3D poses can be generated via simulating the camera re-positioned along the principle axis. Specifically, suppose a 3D point  $(X, Y, Z_0)$  in the original camera coordinate frame with projection at  $(x_0, y_0)$  in the original image is placed at  $(X, Y, Z_1)$  in the new camera coordinate frame and be projected to  $(x_1, y_1)$  in the new image, we can write the following relationships based on similar triangles:

$$\frac{X}{x_1 - cx} = \frac{Z_1}{f} = \frac{Y}{y_1 - cy} \quad (4)$$

$$\frac{X}{x_0 - cx} = \frac{Z_0}{f} = \frac{Y}{y_0 - cy} \quad (5)$$

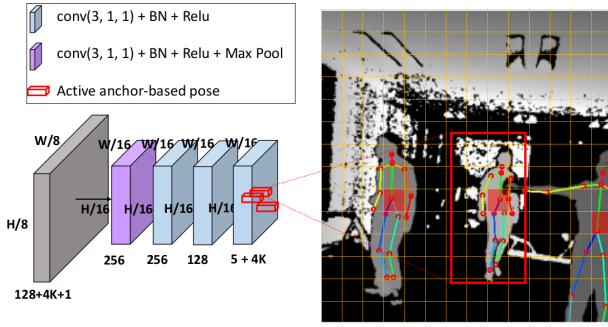


Figure 12: **Global pose network.** The global pose network is composed of four  $3 \times 3$  convolutional layers, where an additional max-pooling is involved in the first layer. The network outputs an anchor-based global pose map, which is converted to a set of poses after NMS.

where  $(cx, cy)$  represents the principle point in both images, and  $f$  indicates the focal length. Dividing the first equation by the second, we get:

$$a = \frac{x_0 - cx}{x_1 - cx} = \frac{y_0 - cy}{y_1 - cy} = \frac{Z_1}{Z_0} \quad (6)$$

Thus, a new depth image can be simply generated via randomly sampling  $a$  within a reasonable range, and mapping the area defined by the original four image corners to the new locations in the new image. Meanwhile, the depth values of the new image and the associated 2D and 3D body part positions can also be calculated. This depth augmentation method is rather effective. However, it can not simulate the dis-occlusion from a different camera location, such that the augmented depth data can not fully represent the quality of real captured data. In practice, the synthesized depth is directly determined by the original depth and  $a$ , whose effect is analysed in Section 4.3.

### C MULTI-PERSON DATA AUGMENTATION

Multi-person and background data augmentation plays an important role in training models generalizable to uncontrolled multi-person scenarios. Such augmentation is enabled by the training data of MP-3DHP, which not only includes ground-truth 3D joint positions but also the foreground masks. Specifically, the training set includes human subjects recorded at four different locations relative to the camera plus a set of free-style movements, as shown in Figure 6 (top) and a set of background-only images as shown in the left two images in Figure 6 (bottom). Given a set of background-only images, a human segment from the training set can be used to simply override the pixels within the same region, leading to a background augmented image as shown in Figure 13 (Top). Similarly, human segments from different recording locations can be composed with random background images following the  $z$ -buffer rule to generate multi-person augmented images as shown in Figure 13 (Bottom).

There are a few heuristics associated with the simple augmentation. First, we include no more than two bodies in the multi-person augmentation with an assumption that inter-person occlusion cases between two bodies can well represent the inter-person occlusion cases between more bodies. Second, the straight-forward composition does not consider scene geometry, thus some generated cases appear unrealistic. However, the conflict with scene geometry is not considered a serious issue in training because all the pipelines only adopt convolutional layers learning that only relies on the local context between a body part and the background in its vicinity rather than the whole scene. Finally, there are sensor artifacts around each human segment that can not be perfectly removed. This issue indeed affects the generalization capability of a trained model to



Figure 13: **Augmented training samples.** (Top) Single-person training samples augmented with a random background scene. (Bottom) Augmented multi-person training sample composed of multiple single-person training samples and a random background scene.

the real data. For example, an occluded part from the augmented data is still roughly visible because of the black margin around the human segment, however an occluded part appears truly invisible in real data. Examples of multi-person augmentation and background augmentation are visualized in Figure 13.

### D APPLICATION

For AR/VR applications, we demonstrate that our prediction of 3D human body parts enables the virtual avatar driving where 3D motion capture plays a key role. As shown in Fig. 14, we convert a sequence of predicted 3D joint positions into the rotation angles of each joint to drive the animated virtual avatar. The supplemental video shows a frame-by-frame avatar-driving animation, and the result is further smoothed by inter-frame filtering. Here, we show the result by recovering the rotation angle of each joint, and the pelvis position is fixed in a certain location.

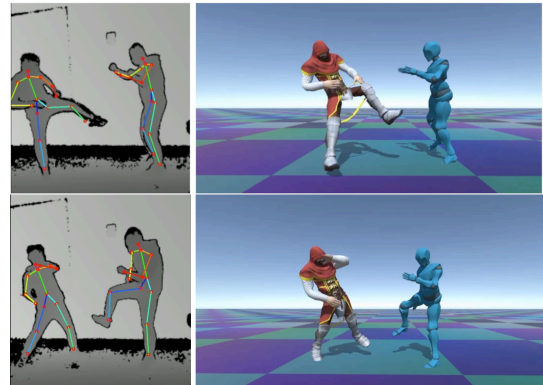


Figure 14: **Virtual avatar driving results.** The left column shows the input depth images and the right column shows the corresponding virtual avatar interaction.